Electronic supplementary material for:

Herzog H, Klein B, Ziegler A. 2017 Form and function of the teleost lateral line revealed using three-dimensional imaging and computational fluid dynamics. *J. R. Soc. Interface*

Extended Methods

Experimental organisms

The ide, a European member of the Cyprinidae (Teleostei: Cypriniformes), has diurnal habits and feeds on plant material as well as various aquatic and terrestrial animals (Kottelat & Freyhof 2007). Ide are commonly found in clear pools of medium to large lowland rivers as well as in ponds and lakes, but have also been reported from brackish estuaries and in coastal waters of the Baltic Sea (Berg 1964). The golden variety of the ide is pale yellow to orange in color, often with dark patches, and has been cultured for ornamental garden ponds (Wheeler 1969).

Light microscopy

Methylene blue is a heterocyclic aromatic chemical conventionally used to visualize neuromast distribution and the lumen of lateral line canals through vital staining.

Micro-computed tomography

Contrast between different tissues was obtained based on the varying uptake of tungsten through diffusion (Metscher 2009).

Terminology

Designation of individual cephalic lateral line canals follows the terminology proposed by Coombs and colleagues (1988): IO = infraorbital canal, MA = mandibular canal, OT = otic canal, PO = postotic canal, POP = preopercular canal, SO = supraorbital canal, ST = supratemporal commissure, T = temporal canal.

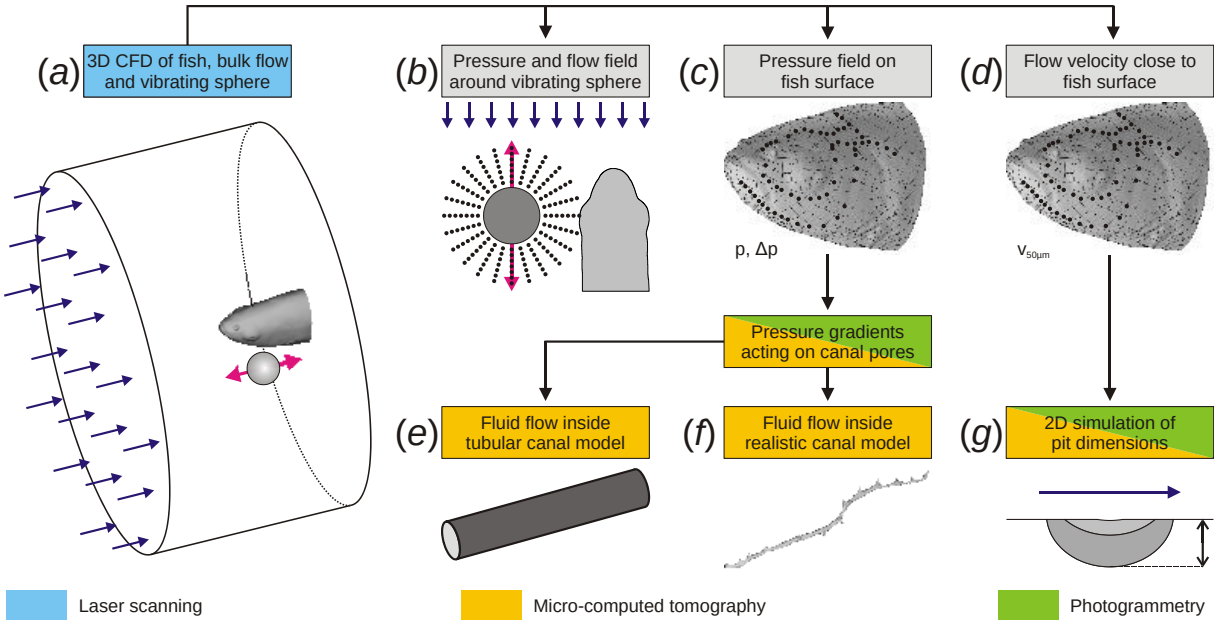

Figure S1. Overview of 3D imaging techniques and simulations used to analyze the cephalic lateral line of *Leuciscus idus*. (*a*) 3D CFD simulation of a vibrating sphere in bulk water flow using a model obtained through laser scanning. (*b*) Simulation of pressure and flow fields surrounding a vibrating sphere placed close to the head. (*c*) Simulation of surface pressures acting on canal pores of the cephalic lateral line. (*d*) Simulation of flow velocity close to canal pores at a distance of 50 µm to the head. (*e*) Simulation of fluid flow inside lateral line canals using a tubular model. *(f)* Simulation of fluid flow inside lateral line canals using a realistic model based on µCT data. *(g)* 2D simulation of the influence of epidermal pits on surface hydrodynamics. Black dots in *(b-d)* represent measuring points.

Setup and properties of the CFD studies

Computational fluid dynamics (CFD) was performed by finite element modeling (FEM) using the commercial software Multiphysics 4.2 (COMSOL Inc., Version 4.2.0.150) running on a personal computer (Intel Core i7 860@2.8 GHz, 16 GB RAM, NVIDIA GeForce GTX 260, Win7 64bit). All simulations used laminar flow models based on the Navier-Strokes equation. More general information on CFD techniques has been published previously (Anderson et al. 1995, Chung 2010, Reddy & Gartling 2010, Ferziger & Peric 2012).

The laser scanning-based model was favored for most 3D CFD simulations, because 1) FEM requires solid shapes, but the fish's 3D model obtained using µCT was not a solid mesh, but rather an ensemble of unrelated vertices with manifold edges and tiny holes, 2) FEM subdivides solid shapes into smaller subcompartments and so the high number of flat vertices in the mesh of the entire animal would have resulted in a large number of finite elements that would have exceeded conventional hardware capabilities, and 3) preparation

of specimens for contrast-enhanced μCT resulted in deformations of some parts of the fish that would have influenced flow field simulations.

3D CFD of fish, bulk flow and vibrating sphere

In terms of the virtual setup and hydrodynamic stimulus conditions, the 3D fluid simulation resembles the electrophysiological studies conducted by Engelmann et al. (2002) and Chagnaud et al. (2007): a fish was placed in a tank featuring laminar incompressible flow directed from snout to tail, while a small sphere placed next to the fish was vibrating parallel to its rostro-caudal axis. The main results of these former studies was that canal neuromasts (CNs) can detect the vibrating sphere signals even when a background flow stimulus is present; in contrast, superficial neuromasts (SNs) can only detect the vibrating sphere in still water, i.e. without additional bulk flow present in the tank. The fluid simulations presented here are aiming to provide new insights into the underlying hydrodynamics.

The 3D simulation featuring a fish, bulk flow, and vibrating sphere used the following two parameters: 1) bulk water directed from the snout to the rear of the fish was flowing with a velocity of 10 cm/s, 2) a sphere vibrating with a frequency of 50 Hz parallel to the fish's midline was generating additional water motion and was placed close to the fish's eye (outline distance to fish 7 mm). The geometry was composed of a cylinder (diameter 120 mm, height 65 mm) representing the experimental tank, one of the 3D models gathered by laser scanning that represented the anterior part of the fish, and a sphere (diameter 10 mm). To create the free water column (temperature 293.15 K, density and viscosity from internal COMSOL database), the fish and the sphere were subtracted from the cylinder (Fig. S2a).

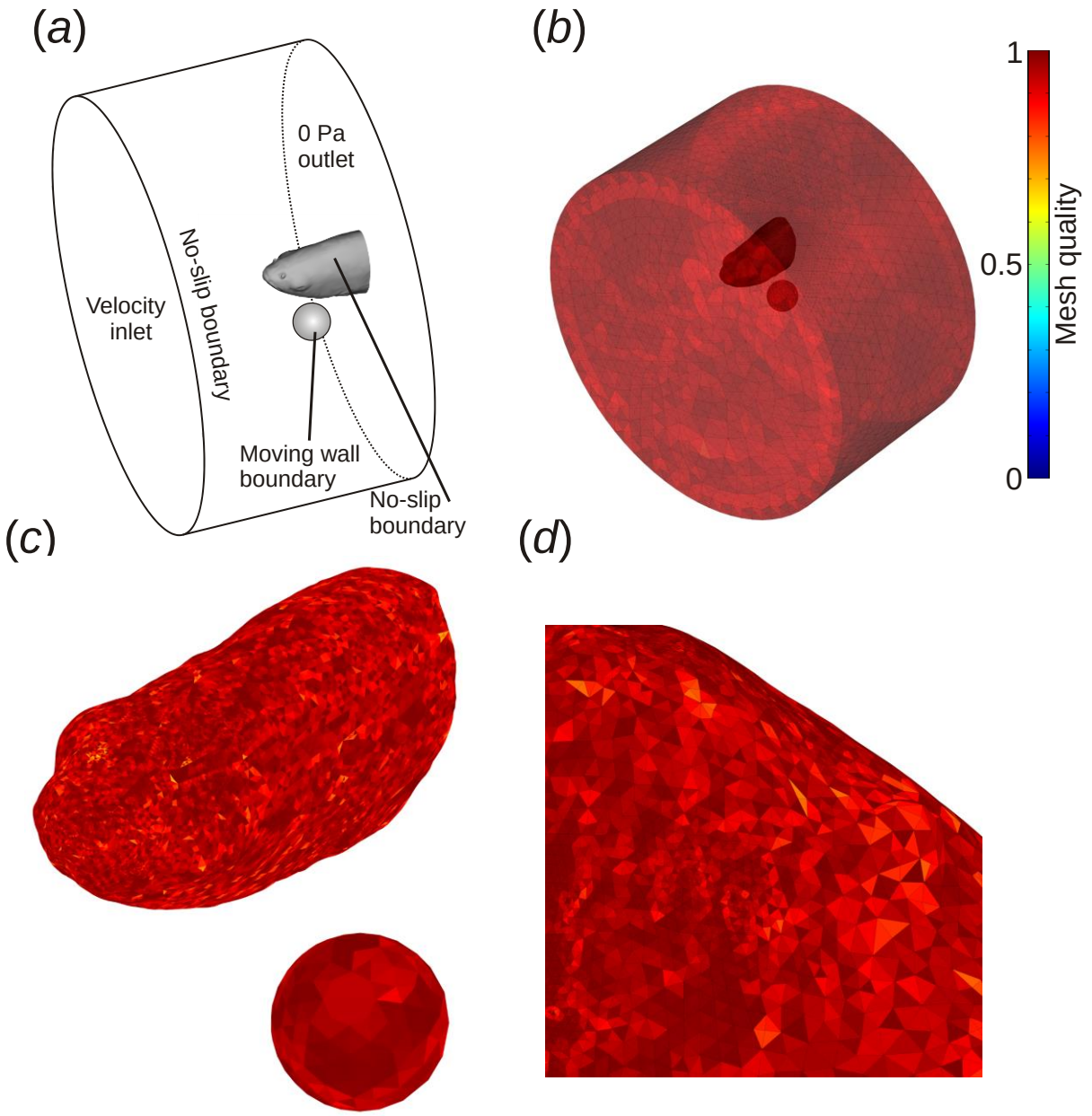

Figure S2: 3D simulation featuring bulk water flow, a vibrating sphere and a fish model obtained using laser scanning. (*a*) Schematic of geometric setup and boundary conditions. *b-d*: FEM mesh quality of the overall setup (*b*), magnified view of fish and sphere (*c*), and a detail of the left-sided ventral snout region (*d*). Mesh quality scale in (*b*) also applies to (*c*) and (*d*).

The resulting FEM mesh featured 1,095,043 elements (Fig. S2b). Although the 3D fish model had a complex curved shape, the FEM mesh of its surface had a good overall quality (Fig. S2c). However, some small sections of the model had a slightly degraded mesh quality and a large spread of element size, e.g. in the ventral snout region (Fig. S2d).

The following boundary conditions were used in this 3D simulation: 1) the fish surface featured a no-slip, tetrahedral boundary layer, 2) the end face of the cylinder anterior to the fish was set to a velocity inlet featuring 10 cm/s, 3) the end face of the cylinder posterior to

the fish was set as 0 Pa pressure outlet, 4) the side walls of the cylinder featured a no-slip, tetrahedral boundary layer, 5) the sphere surface used moving wall condition and two prismatic boundaries (COMSOL boundary function). Sinusoidal sphere displacements of ±2 µm, ±10 µm, ±50 µm, and ±150 µm at a vibration frequency of 50 Hz (equation: wall velocity = displacement*sin(2π*50°Hz*t)*2π*50°Hz; displacement = 2 µm, 10 µm, 50 µm, and 150 µm) were generated by the moving wall condition.

Independent studies were performed for the four displacement amplitudes. In each of them, a mathematical solution to the hydrodynamic problem was found by two consecutive steps resulting in 785,504 degrees of freedom: a stationary solution was computed to describe the general fluid dynamics caused by the bulk water flow directed from snout to tail of the fish and a second, time-dependent study including 2.7 cycles of sphere vibration (0 to 0.054 s, intermediate time stepping with a step size of 0.1 ms) that used the stationary solution as starting point. Fully-coupled (u, p) GEMRES solvers were used in the stationary and time-dependent study. For each of the four displacement amplitudes, the computation time was about 40 h.

The resulting flow velocity and pressure fields surrounding the vibrating sphere were estimated in a plane along 24 directions and at distances from the sphere's outline of 1 to 7 mm. To evaluate a possible stimulation of SNs by bulk water flow and the vibrating sphere, the flow velocity was examined for positions close to each canal pore at an approximated distance of 50 µm from the fish's surface (McHenry & van Netten 2007). Similarly, pressure was evaluated for positions where canal pores were present in the real fish. Pressure gradients along the segments of the lateral line canals were calculated by subtracting the pressure amplitudes measured on adjacent pores. For each evaluation point (sphere, pores, or canal segments), measured values (velocity, pressure, difference pressure) within the last cycle of sphere vibration were fitted by a sinusoidal function (least square method, nonlinear GRP solver, Microsoft Excel 2010) according to the equation:

$$p; v = a + b \times \sin(t + c)$$

Where *p*;*v* is the measured pressure;velocity, *t* is simulation time, *a* is the vertical offset of the sine function, *b* is the sine amplitude (*b* constrained to be positive) and *c* is phase/horizontal offset.

Coefficient *a* corresponds to the peak of the sinusoidal variation of the signals induced by the vibrating sphere. Coefficient *b* corresponds to the DC signal induced by the bulk water flow. Coefficient *c* corresponds to the phase of the sinusoidal variation of the signals induced by the vibrating sphere. The relative sphere signals (i.e. the modulation depth of the DC velocity and pressure magnitudes) were examined by dividing coefficient *b* by coefficient *a*, i.e. AC sphere signal by DC bulk flow signal.

Fluid flow inside tubular canal model

Fluid flow inside the cephalic lateral line canal system was approximated using a simplified tubular model. Due to the rotational symmetry of the simulation geometry, a revolved 2D geometry featuring a rectangle was used for this simulation and resulted in a mathematical solution for the simulated cylindrical canal segment (Fig. S3a). To represent the noteworthy variations in canal dimensions found in the ide, the dimensions of the revolved rectangles were altered in length (1 mm, 1.5 mm, 2 mm) and width (i.e. half of the resulting canal diameter: 19.5 µm, 54 µm, 88 µm) resulting in nine tubular geometries (Fig. S3b). The total number of FEM mesh elements varied as a function of rectangle dimensions. In case of a canal diameter of 108 µm and a length of 1 mm, the FEM mesh contained 15,696 2D elements. (Fig. S3c, d).

In each model, the side walls of the canal featured no-slip boundary conditions and two quad element layers (COMSOL boundary function). To apply sinusoidal pressure variations superimposed on a DC signal, one end of the rectangle was set as a pressure inlet (pressure = 1 Pa+sin(2π*50 Hz*t)*0.1 Pa) and the opposite end was defined as a 0 Pa pressure outlet. The area of the rectangle, i.e. the resulting fluid volume of the cylindrical canal model, was defined as canal fluid (dynamic viscosity: 5.1 mPa*s estimated by van Netten & Kroese (1987) and the density of water) featuring laminar compressible flow (Ma<0.3).

The time-dependent study for 2.7 cycles of the alternating pressure signal (0 to 0.054 s, intermediate time stepping with a step size of 0.1 ms) used the PARADISO solver. Sinusoidal fitting of canal fluid velocity was performed for the last cycle of the alternating pressure signal using the cross-section average of the revolving canal at half of the canal length (fit function described above).

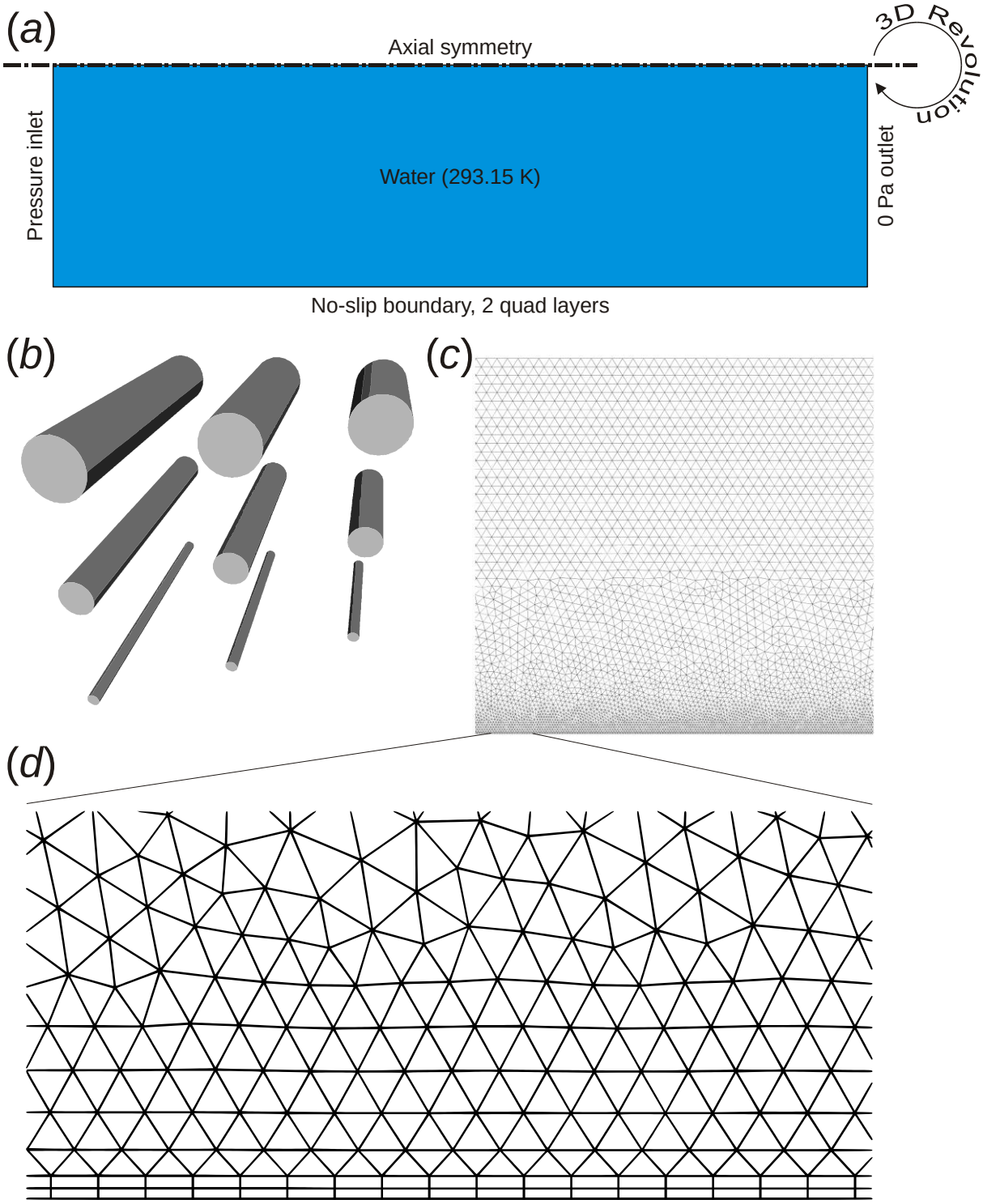

Figure S3: Simulation of fluid flow inside the lateral line canals by means of a cylindrical model. (*a*) Schematic of the cylindrical simulation geometry (not to scale). (*b*) Variation of canal dimensions present in the ide investigated by a cylindrical canal model. (*c*) FEM mesh of the cylindrical canal (diameter 108 µm, length 1 mm). (*d*) Magnification of the outer boundary of the mesh (canal wall).

Fluid flow inside the supraorbital canal (SO)

The fluid flow inside lateral line canals induced by pressure gradients was also estimated by means of an isolated canal section of the supraorbital canal (SO) that was obtained from segmentation data of the contrast-enhanced µCT scan. The canal model featuring 5,000 vertices was exported from the software Amira as a stereolithography (STL) file. The structure was imported into COMSOL Multiphysics (Fig. S4a). This reduced representation resulted in a FEM mesh featuring 1,025,406 elements and an overall adequate quality. However, individual vertices of the model had - presumingly due to small dimensions and/or angular placement to adjacent vertices - a degraded mesh quality (Fig. S4b).

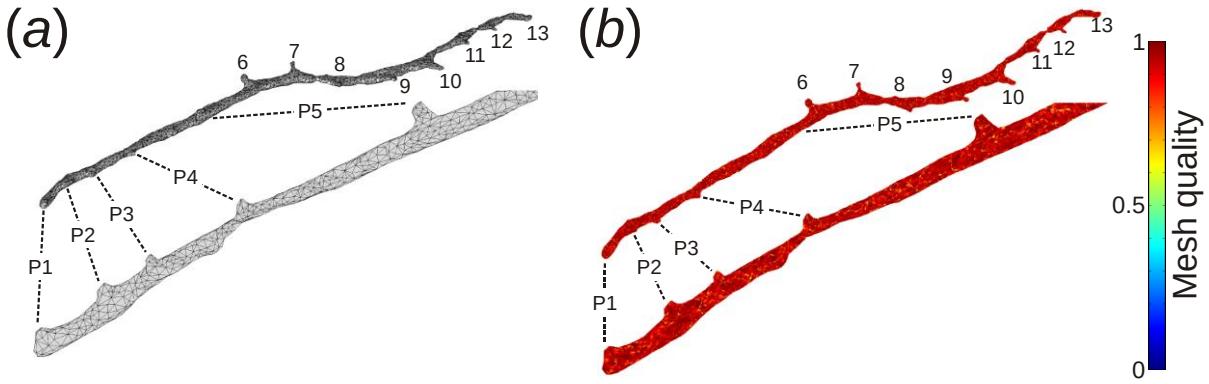

Figure S4: 3D simulation of the actual geometry of the SO. (*a*) Rostro-lateral view of the canal geometry obtained from µCT-based manual segmentation of the canal's lumen. (*b*) Corresponding FEM mesh quality. P1-P5 = pore 1-5.

According to the observations made in the µCT investigations and the results of the first simulation, some facets at positions where the 13 canal pores were present in the real fish were set as pressure inlets (Fig. S4a). Time-dependent pressure amplitudes were derived from corresponding measuring points in the first simulation and +/-50 µm displacement amplitude. A scaling factor was introduced to describe the other displacement amplitudes according to the equation below (Tab. S1).

$$p = a + s \times b \times \sin(t + c)$$

p	Pressure in Pa
t	Time in seconds
s	Sphere displacement factor (s = 0.04 for +/-2 µm, s = 0.2 for +/-10 µm, s = 1 for +/-50 µm, s = 3 for +/-150 µm)
a	Offset coefficients of fit function (see below)
b	Scale coefficients of fit function (see below)
c	Phase coefficients of fit function (see below)

Table S1: Coefficients of pressure values applied to pores of SO model.

Pore	***a* (offset)**	***b* (scale)**	***c* (phase)**
1	1.7748441395311300	0.6743745801851020	0.0049291837062134
2	0.7537136156402150	0.6214476974730820	0.0049777135900822
3	-0.2584983359596540	0.5863088601939390	0.0050122746047285
4	-0.6137234646154030	0.5372322741879780	0.0050631765463413
5	-0.3728989220308350	0.3594917247134640	0.0051815844707856
6	-0.4734270409172590	0.2400951232473340	0.0053443602419661
7	-0.4891829406764670	0.1377658809496640	0.0056724461090753
8	-0.7004129843269410	0.0617496941043087	0.0073779135725208
9	-0.7771624576667320	0.0950739091392113	0.0134868141533641
10	-0.8643194027222380	0.2044525120291030	0.0141788206381658
11	-0.7917179194121400	0.3012879065201370	0.0144686869125146
12	-0.5832623638866240	0.3053089179933560	0.0146197155054044
13	-0.4781114683691070	0.3366336959671470	0.0147121296176050

The remaining facets of the model featured no-slip boundary conditions and a tetrahedral boundary layer. The lumen of the SO model was defined as canal fluid (compressible flow, Ma<0.3, dynamic viscosity: 5.1 mPa*s estimated by van Netten & Kroese (1987) and the density of water). The study was computed using a fully-coupled (u, p) GEMRES solver. Results were visualized by pressure gradients along the canal segments and the flow velocity along selected canal cross sections. As described above, sinusoidal fitting was performed for the average velocity along the cross sections and relative sphere signals were estimated.

2D simulation of epidermal pit dimensions

The influence of the small pits located on the surface of the fish on local fluid flow was investigated by a 2D simulation featuring a parametric sweep of pit depth. The geometry of the simulation was generated by two rectangles and a circle (Fig. S5a). The absolute position of the circle (diameter 500 µm) and the larger rectangle (width 100 mm, height 20 mm) was kept constant during the geometry sweep of the pit depth. As a consequence, spatially fixed evaluation points, e.g. at the SN position on the bottom of the pit, could be used. To alter pit depth from 10 to 450 µm (10 µm, 30 µm, 50 µm, 70 µm, 90 µm, 120 µm, 150 µm, 200 µm, 250 µm, 300 µm, 350 µm, 400 µm, 450 µm), a second rectangle reflecting the skin of the animal (width 100 mm, height 2 mm) was placed vertically shifted to the large rectangle (Fig. S5a). The column of water (T = 293.15 K, compressible flow, Ma<0.3) was created in three consecutive steps: 1) the circle was subtracted from the small rectangle, 2) small fillets (radius 5 µm) were added to the upper edge of the pit, and 3) the resulting geometry was subtracted from the large rectangle. The number of FEM mesh elements varied with pit depth (e.g. 131,731 2D elements for a pit depth of 250 µm).

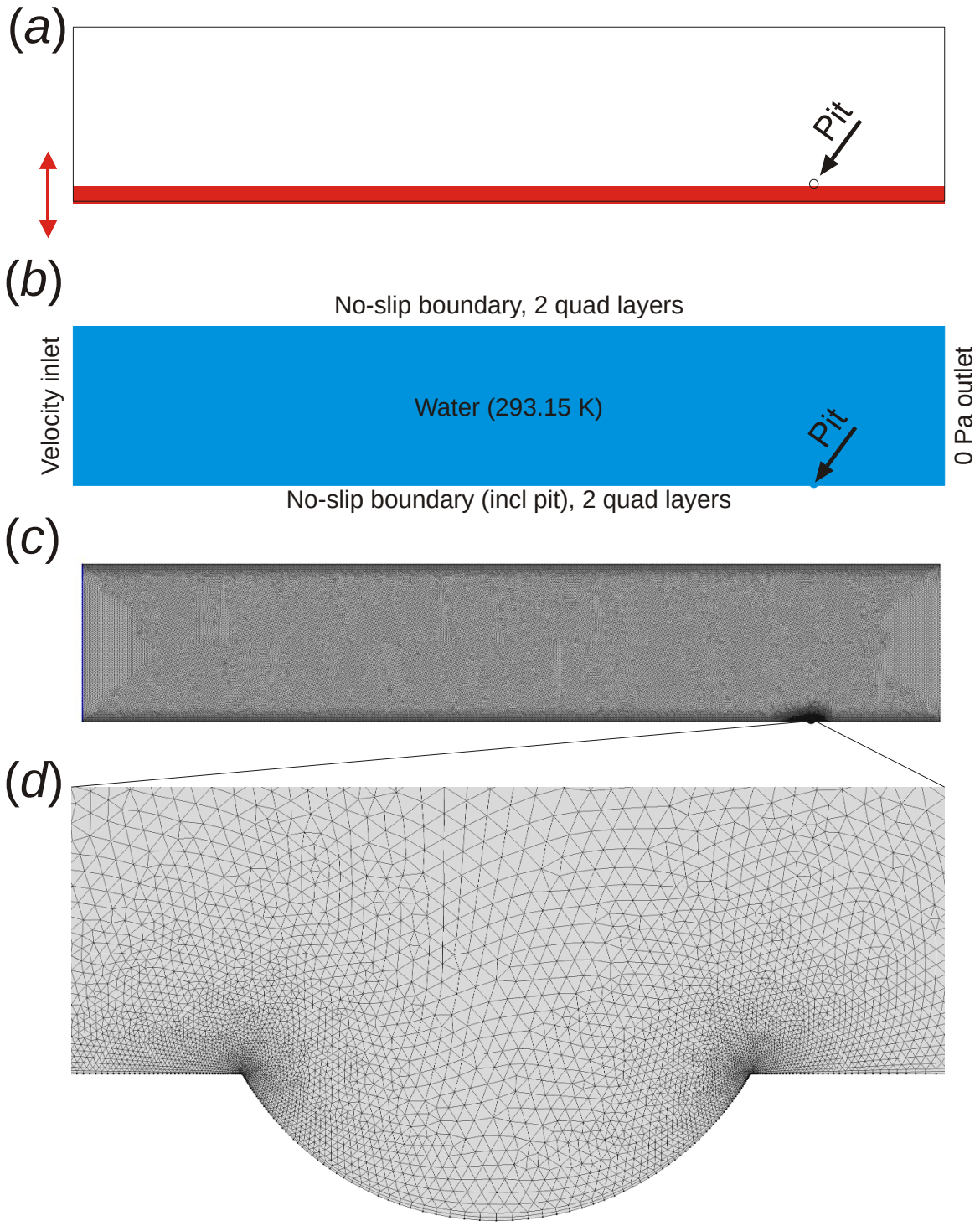

Figure S5: 2D simulation of an epidermal pit. (*a*) Generation of the pit model geometry. Red two-headed arrow indicates vertical shift of the smaller rectangle that altered pit depth. (*b*) Boundary conditions of the pit model. (*c*) FEM mesh of the geometry. (*d*) Magnified view of the FEM mesh at the location of the pit featuring a depth of 250 µm.

In the model, the lower edge (skin surface featuring pit) as well as the upper edge of the fluid were defined as a no-slip boundary featuring two quad boundaries (COMSOL boundary function). The right edge was defined as the 0 Pa outlet (Fig. S5b). The left edge of the fluid

was defined as the velocity inlet and had a distance of 85 mm to the pit in order to achieve a well-established flow profile at the measuring position. To avoid excessive file size due to additional sweeping of pit depth, the effect of the small pits on bulk flow (DC) and altered flow (25 Hz, 50 Hz, 100 Hz, 200 Hz) was investigated by two separate simulations. The investigations of the DC flow properties applied static velocities ranging from 1 to 101 mm/s (step size of 5 mm/s). The survey on frequency filtering used alternating velocity signals superimposed on bulk flow (velocity = 10 mm/s+sin(2π*frequency*t)*0.010 mm/s; frequency: 25 Hz, 50 Hz, 100 Hz, or 200 Hz).

For each flow velocity, a stationary study featuring a geometry sweep of pit depth was solved to investigate the bulk flow (DC) in the surroundings of the small pits. In case of the investigation of frequency filtering, two consecutive steps were used for each pit depth: a stationary solution was computed to describe the general fluid dynamics caused by the bulk flow along the fish surface and a second, time-dependent study including four cycles of alternating signal (intermediate time stepping with a step size of 1/200 cycle) that used the stationary solution as starting point. Fully-coupled (u, p) PARADISO solvers were used in both the stationary and the time-dependent study of the DC as well as the frequency filtering examinations. Fluid flow velocity was evaluated along the center of the pit at heights of 0 to 1 mm as measured from the bottom of the pit. For each evaluation point, velocity values within the last cycle of sphere vibration were fitted by the sinusoidal function to estimate AC (sphere) and DC (bulk flow) signals as well as the ratio between both.

Data repository

As mentioned in the article, raw data associated with this publication have been deposited and are available for download (Herzog et al. 2017). Please use the ‘Media’ and ‘Documents’ tabs of this MorphoBank project.

Extended Results

Morphometric measurements

Table S2: Counts of cephalic lateral line canal pores in *Leuciscus idus.*

Body side	SO	IO	MA/POP	OT/PO/T	ST	Total
Left	12	16	20	8	4.5	60.5
Right	13	13	18	10	4.5	58.5

The values were obtained using µCT data of a specimen with 6.3 cm TBL. IO = infraorbital canal, MA = mandibular canal, PO = postotic canal, POP = preopercular canal, OT = otic canal, SO = supraorbital canal, ST = supratemporal commissure, T = temporal canal.

Table S3: Diameter of cephalic lateral line canals in *Leuciscus idus*.

Plane	SO (left)	SO (right)	IO (left)	IO (right)	MA (left)	MA (right)
1	-	-	85	127	111	126
2	103	145	101	114	135	123
3	120	151	81	107	105	116
4	75	123	54	101	109	105
5	128	130	88	95	130	141
6	176	85	113	78	113	95
7	151	109	39	107	84	60
8	101	109	94	96	151	62
9	112	144	85	96	92	109

The values were obtained using µCT data of a specimen with 6.3 cm TBL. The location of planes 1-9 is shown in Figure 3b. Values are provided in µm. IO = infraorbital canal, MA = mandibular canal, SO = supraorbital canal.

Table S4: Number of epidermal pits and SNs found on the head of *Leuciscus idus*.

Structure	In front of the eye	Above the eye	Below the eye	On ventral side of the mandible	Behind the eye	On the operculum
Epidermal pit (this study)	22	47	75	10	13	0
SN (this study)	23	79	108	10	30	56
SN (Schmitz et al. (2014))	43	71	105	12	38	82

The values obtained in this study using specimens with a TBL of 6.3 cm (µCT, CNs) and 7 cm (light microscopy, SNs) are compared with data previously obtained using a specimen with 9 cm TBL (Schmitz et al. 2014). The terminology follows these authors. SN = superficial neuromast.

Table S5: Measurements of epidermal pit dimensions in *Leuciscus idus*.

Dimensions	30 x 30	30 x 40	30 x 50	40 x 30	40 x 40	50 x 40	50 x 50	50 x 60	60 x 40	60 x 50	70 x 40	70 x 50	70 x 60
Epidermal pit number (dorsal)	20, 22	18	15	13, 19	14, 16, 17, 21, 24	11, 12, 25	23	10	2, 3	1, 6, 8	5	4, 7	9
Dimensions	40 x 20	40 x 30	50 x 20	50 x 30	50 x 50	60 x 30	60 x 40	60 x 50	70 x 30	70 x 40	70 x 50	80 x 60	
Epidermal pit number (lateral)	18, 20	15	16, 17, 19	12, 14, 21, 25	4	10, 11, 23, 24	8, 9	2, 3	22	6, 7, 13	1	5	

The values were obtained using a µCT dataset with 5 µm isotropic voxel resolution of a specimen with 6.3 cm TBL. A dorsal and a lateral transect were measured, with epidermal pit 1 always being the most anterior. Distance between pits was about 1 mm. The dimensions (width x depth, first and third line) are provided in µm.

References

Anderson Jr. JD, Degroote J, Degrez G, Dick E, Grundmann R, Vierendeels J. 1995 Computational Fluid Dynamics, Volume 206 (ed J Wendt). New York: McGraw-Hill, XX pp.

Berg LS. 1964 Fresh Water Fishes of the USSR and Adjacent Countries II. Jerusalem: I.P.S.T., 492 pp.

Chagnaud BP, Hofmann MH, Mogdans J. 2007 Responses to dipole stimuli of anterior lateral line nerve fibres in goldfish, *Carassius auratus*, under still and running water conditions. *J. Comp. Physiol. A* 193, 249-263.

Chung TJ. 2010 Computational Fluid Dynamics. Cambridge: University Press, 1058 pp.

Coombs S, Janssen J, Webb J. 1988 Diversity of lateral line systems: evolutionary and functional considerations. In Sensory Biology of Aquatic Animals (eds J Atema, RR Fay, AN Popper, WN Tavolga). New York: Springer, pp. 553-593.

Engelmann J, Hanke W, Bleckmann H. 2002 Lateral line reception in still- and running water. *J. Comp. Physiol. A* 188, 513-526.

Ferziger JH, Peric M. 2012 Computational Methods for Fluid Dynamics. Berlin: Springer Science & Business Media, 423 pp.

Herzog H, Klein B, Ziegler A. 2017 Form and function of the teleost lateral line revealed using three-dimensional imaging and computational fluid dynamics. MorphoBank project 2542. DOI: http://dx.doi.org/10.7934/P2542

Kottelat M, Freyhof J. 2007 Handbook of European Fresh Water Fishes. Berlin: Kottelat, Cornol and Freyhof, 646 pp.

McHenry MJ, van Netten SM. 2007 The flexural stiffness of superficial neuromasts in the zebrafish (*Danio rerio*) lateral line. *J. Exp. Biol.* 210, 4244-4253.

Metscher BD. 2009 MicroCT for comparative morphology: simple staining methods allow high-contrast 3D imaging of diverse non-mineralized animal tissues. *BMC Physiol.* 9, 11.

Reddy JN, Gartling DK. 2010 The Finite Element Method in Heat Transfer and Fluid Dynamics. Boca Raton, FL: CRC Press, 524 pp.

Schmitz A, Bleckmann H, Mogdans J. 2014 The lateral line receptor array of cyprinids from different habitats. *J. Morphol.* 275, 357-370.

van Netten SM, Kroese AB. 1987 Laser interferometric measurements on the dynamic behaviour of the cupula of the fish lateral line. *Hear. Res.* 29, 55-61.

Wheeler A. 1969 Fishes of the British Isles and North-west Europe. London: Macmillan, 672 pp.